Global Biogeochemical Cycles

RESEARCH ARTICLE
10.1029/2020GB006764

Key Points:

- Submesoscale dynamics enhance the contribution of slow-sinking particles to particulate organic carbon (POC) export, especially for steep particle size-spectrum slopes
- Remineralization processes intensify the role of slow-sinking particles, to the point where these particle sometime dominate POC export

Correspondence to:
M. Dever,
mdever@whoi.edu

Citation:
Dever, M., Nicholson, D., Omand, M. M., & Mahadevan, A. (2021). Size-differentiated export flux in different dynamical regimes in the ocean. *Global Biogeochemical Cycles*, *35*, e2020GB006764. https://doi.org/10.1029/2020GB006764

Received 29 JUL 2020
Accepted 10 FEB 2021

Size-Differentiated Export Flux in Different Dynamical Regimes in the Ocean

M. Dever[1], D. Nicholson[1], M. M. Omand[2], and A. Mahadevan[1]

[1]Physical Oceanography Department, Woods Hole Oceanographic Institution, Woods Hole, MA, USA, [2]Graduate School of Oceanography, University of Rhode Island, Narragansett, RI, USA

Abstract Export of Particulate Organic Carbon (POC) is mainly driven by gravitational sinking. Thus, traditionally, it is thought that larger, faster-sinking particles make up most of the POC export flux. However, this need not be the case for particles whose sinking speeds are comparable to the vertical velocities of a dynamic flow field that can influence the descent rate of particles. Particles with different settling speeds are released in two process-oriented model simulations of an upper ocean eddying flow in the Northeast Pacific to evaluate the impact of (1) ocean dynamics on the respective contribution of the different sinking-velocity classes to POC export, and (2) the particle number size-spectrum slope. The analysis reveals that the leading export mechanism changes from gravitationally driven to advectively driven as submesoscale dynamics become more active in the region. The vertical velocity associated with submesoscale dynamics enhances the contribution of slower-sinking particles to POC export flux by a factor ranging from 3 to 10, especially where the relative abundance of small particles is large (i.e., steep particle size-spectrum slope). Remineralization generally decreases the total amount of biomass exported, but its impact is weaker in dynamical regimes where submesoscale dynamics are present and export is advectively driven. In an advectively driven export regime, remineralization processes counter-intuitively enhance the role of slower-sinking particles to the point where these slower-sinking velocity classes dominate the export, therefore challenging the traditional paradigm for POC export. This study demonstrates that slow-sinking particles can be a significant contribution, and at times, even dominate the export flux.

1. Introduction

Photosynthesis in the sunlit upper ocean and the production of Particulate Organic Carbon (POC) takes up dissolved inorganic carbon and facilitates the uptake of CO_2 from the atmosphere. The sinking of POC exports organic carbon from the upper ocean to the interior, leading to the sequestration of carbon (Boyd et al., 2019; Falkowski et al., 1998) on timescales ranging from days to years depending on the sinking depth and circulation. Despite progress on sampling and viewing particles in the ocean, direct measurements of particles sinking velocities are difficult to obtain, and often inferred from key parameters such as particle type, size, and density (McDonnell & Buesseler, 2010, 2012).

Traditionally, POC export is thought to occur through gravitational sinking and one-dimensional models have been used to describe the sinking POC flux with depth (Armstrong et al., 2001; DeVries et al., 2014; Jackson et al., 1997; Omand et al., 2020). Particles produced through primary and secondary production in the surface layer that are relatively large and fast sinking tend to sink out of the upper surface layer on timescales shorter than the timescale on which the particles get remineralized. It is reasonable to treat POC export as sinking-dominated if the vertical advective velocities in the ocean are weaker than the velocities associated with gravitational sinking. However, Particulate Organic Matter (POM) has a wide range of particle shape, size and type, that results in particle sinking velocities ranging from practically zero, to several hundreds of meters per day (Baker et al., 2017; Riley et al., 2012). The size spectrum, or number distribution of particle sizes, is usually characterized by a power law with the power ranging between −2 and −4, for which the abundance of small particles is $\mathcal{O}(10^4 - 10^8)$ greater than large particles (McCave, 1984; Petrik et al., 2013). The biomass size spectrum, which indicates the distribution of biomass versus particle size, tends to be flatter and variable in shape (Sheldon et al., 1972) compared to the particle number spectrum, because the volume (and mass) of a particle scales with its linear size raised to a power that exceeds 1 (and typically varies between two and three depending on shape and porosity). Importantly, it means that a

significant fraction of the particulate biomass is in the small size fraction (Richardson & Jackson, 2007). Even though the sinking velocity w_s of particles does not perfectly relate to particle size l, it is fair to assume that $w_s \sim l^n$ (with $n = 2$ according to Stokes law, and $1 < n < 2$ for complex particle shapes). Due to this, as well as the fact that particles of organic matter are not very much greater in their densities than seawater, a significant fraction of the biomass sinks very slowly (at velocities less than tens of meters per day). When the gravitational sinking velocity of particles is comparable to (or smaller than) the vertical velocities in the flow field, the dynamics of the flow field can impact the trajectories and fate of the POC. Thus, depending on the flow dynamics, and the fraction of slow-sinking particulate biomass, the sinking of organic matter can be affected by the fluid flow in the ocean.

Recent studies have shown that ocean dynamics can play a role in driving the transport of carbon from the euphotic layer to the ocean interior (Llort et al., 2018; Stukel & Ducklow, 2017; Stukel et al., 2018). For example, enhanced vertical velocities along the edge of a mesoscale eddy led to a funneling of particles along the eddy's periphery (van Haren et al., 2006; Waite et al., 2016) and in mesoscale features in the California current (Stukel et al., 2017). Omand et al. (2015) found that submesoscale mixed layer eddies, while contributing to the restratification of a frontal zone, were subducting a large amount of nonsinking POC from the surface productive layer during the onset of the spring bloom in the subpolar North Atlantic. Advectively subducting plumes or filaments of high oxygen, chlorophyll and small POC (evidenced through backscatter) were detected from a suite of gliders during the North Atlantic Bloom experiment (Alkire et al., 2012). Using model simulations to capture the process of eddy-driven subduction, Omand et al. (2015) estimated the downward advective flux of nonsinking POC and parameterized it. Briggs et al. (2011) quantified the flux of fast-sinking particles consisting largely of diatoms from observations of optical backscatter. But, these estimates did not account for a range of sinking particle velocities. Typically, POM has a wide spectrum of sinking velocities and in order to understand its fate and export, we need to consider the biomass distribution as a function of the particle sinking velocity spectrum and its interaction with the dynamics of the flow field in the ocean.

A growing body of literature focusing on submesoscale (1–10 km) dynamics is exploring its impact on biogeochemical processes (Lévy et al., 2012; Mahadevan, 2016). Submesoscale dynamics, characterized by Rossby numbers of order 1, typically develop in filaments in areas where sharp density fronts exist (Klein & Lapeyre, 2009; McWilliams, 2016; Thomas, Taylor, et al., 2013). In this dynamical regime, geostrophic balance breaks down and a secondary ageostrophic circulation develops across the front, capable of generating large vertical velocities on the order of 100 m/day (Fox-Kemper et al., 2008; Mahadevan, 2016). On the denser side of the front, the vorticity is cyclonic and associated with downwelling velocities, while anticyclonic vorticity and upwelling is expected on the lighter side of the front. The distribution of relative vorticity associated with submesoscale dynamics near the surface exhibits an asymmetry with higher values of positive vorticity than negative vorticity (Rudnick, 2001), leading to more localized and more intense downwelling regions, as opposed to weaker and larger scale upwelling regions (Mahadevan & Tandon, 2006). Enhanced vertical velocities can aid to supply nutrients to the sunlit layer of the ocean for primary production (Lévy et al., 2001; Mahadevan & Archer, 2000) or can significantly increase the export of POC to the ocean interior through localized downwelling (Estapa et al., 2015; Gruber et al., 2011; Lévy et al., 2012; Omand et al., 2015), a process that might not be captured if submesoscales O (1 km) are not fully resolved (Resplandy et al., 2019). The downwelling velocities $\mathcal{O}$(100 m/day) generated at submesoscales provide a physical mechanism for exporting slow sinking or neutrally buoyant particles on timescales shorter than their remineralization timescales. If the fraction of biomass associated with such slow sinking velocities is significant, submesoscale dynamics can potentially impact the export of POC.

We rely on a submesoscale-resolving, nonhydrostatic ocean model to simulate the dynamics in the upper few hundred meters of the ocean. The dynamical model is coupled with a particle-tracking module to model the advection of particles by fluid flow, while neglecting the effects of particle inertia and drag on their advection. In addition, the particles sink with a range of sinking velocities (between 0.025 and 5 m day^{-1}) that is based on the range of vertical currents modeled in this region. We aim to address the transitional regime of the particle sinking velocity spectrum, where both advection and sinking speeds have similar order of magnitude. A similar study with sinking tracers showed the influence of the flow (Taylor et al., 2020), but the use of particles enables a characterization of export associated with each sinking class of particles.

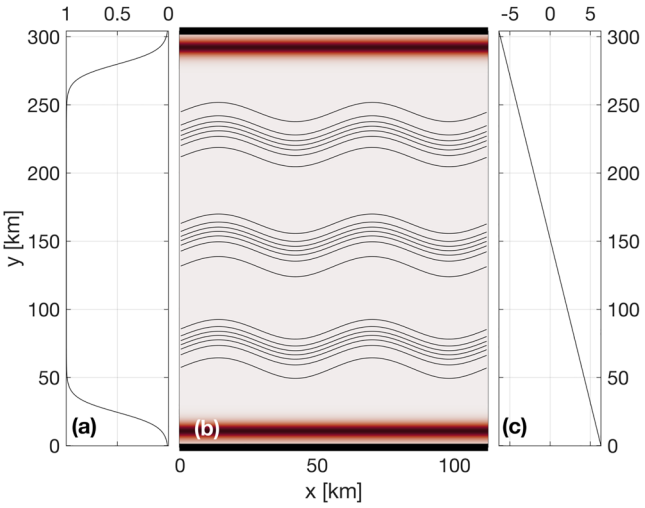

Figure 1. Process Study Ocean Model (PSOM) model setup. (a) Meridional profile of scaling coefficient that multiplies the time-varying zonal wind stress τ_x shown in Figure 3a. The taper at north and south boundaries prevents "coastal" up-/down-welling being entirely concentrated in the boundary grid cell. (b) Restoration factor (color shading) used to dampen internal wave reflection at boundaries as well as up-/down-welling due to the windstress curl. Surface density contours (black) show the three fronts used to initialize the model. (c) Meridional variation of the time-dependent surface heat flux (Figure 3a) prescribed over the domain.

The model is used to quantify the contribution of slow-sinking particles to carbon export, as a function of (1) the dynamics of the flow field, (2) the slope of the sinking velocity spectrum, and (3) the remineralization timescale. Particles in the model are prescribed with both a constant and time-varying sinking velocity to mimic a remineralizing behavior. Particles are released in two fundamentally different flow fields in terms of dynamics based on observed conditions in the Northeast Pacific: In the summer, where ocean dynamics are characterized by low Rossby numbers and weak vertical advective velocities, and in the winter, where ocean dynamics include submesoscale frontal structures and local Rossby numbers $\mathcal{O}(1)$. Both simulations and the particle-tracking module are described in Section 2. The impact of particles characteristics and ocean dynamics on the export of POC is quantified in Section 3, and discussed in Section 4. Section 5 summarizes the key conclusions of the study.

2. Methods

2.1. Model Setup and Domain

This study uses a nonhydrostatic, three-dimensional, Process Study Ocean Model (PSOM; Mahadevan et al., 1996a, 1996b) to simulate an eddy field that is representative of the Northeast Pacific Ocean. The model is set in a channel configuration with periodic east-west boundaries, and solid boundaries in the south and north. The domain covers 112 km in the x-direction, 304 km in the y-direction, and 1,000 m in the vertical (Figure 1). The horizontal resolution is 500 m, while a stretched grid is used in the vertical with 32 levels ranging in thickness from 1.25 m near the surface to 70 m at the lowermost level. The model is integrated numerically in time and evolves the temperature, salinity, free-surface height, pressure, and three-dimensional velocity field from an initial state, subject to momentum and buoyancy fluxes applied through the surface boundary.

Time-varying wind stress and heat flux are prescribed at the surface boundary. Time series are computed from measurements collected at Station Papa and available through the Pacific Marine Environmental Laboratory (PMEL, 2018). Daily wind stress and net heat fluxes are calculated over the period 2007–2016 to produce a year-long climatology. A squared low-pass filter with a cut-off frequency of 8.5 days is applied to both time series to remove high-frequency variability. In all numerical experiments, simulations are run for the first 5 days without any forcing applied to the surface boundary. Surface wind stress and heat fluxes are then linearly ramped up between days 5 and 10 of the simulation, to reach realistic values at day 10.

While the meridional component, τ_y, is set to zero, the zonal component of the wind stress, τ_x, is prescribed at the surface throughout the model domain and is tapered at the northern and southern boundaries to avoid excessive Ekman-driven upwelling and downwelling (Figure 1a). A restoration timescale is prescribed to contain the curl-driven upwelling and downwelling regions generated by the tapering of the wind stress, as well as to limit internal wave reflection at the solid boundaries back into the domain (Figure 1b). While net surface heat fluxes are homogeneous in the zonal direction, a meridional gradient is maintained throughout the simulation. The meridional gradient was determined from the North American Regional Reanalysis (NARR) product (Mesinger et al., 2006), and set to 1/24 W/m^2/km (Figure 1c).

Initial hydrographic conditions are determined from a three-dimensional gridded field of temperature and salinity from Argo floats (Gaillard, 2015; Gaillard et al., 2016). Argo data is averaged monthly over the period 2002–2012 and two different months are used to initialize the two main numerical experiments for this study: Climatological conditions in April are used to initialize the *Papa_summer* experiment, while January climatological conditions are used to initialize the *Papa_winter* experiment (Table 1). The north-south background density gradient is then intensified into three fronts located at $y = 75$, $y = 150$, and $y = 225$ km (Figure 1). The amplitude of the density gradient associated with the three fronts is determined from the

Table 1
Summary of the Key Characteristics of PSOM Experiments Papa_summer and Papa_winter

	Papa_summer	*Papa_winter*
Time period	April–July	January–March
Spin-up	60 days	50 days
Advective timestep	216°s	108°s
Horizontal diffusivity	1 $m^2\ s^{-1}$	0.2 $m^2\ s^{-1}$
Restoration timescale	3 days	15 days
Zonal wind stress	0 – +0.16°N m^{-2}	−0.05 – +0.17°N m^{-2}
Surface heat flux	−46.8 – +167.5 W m^{-2}	−57.6 – +15.3 W m^{-2}
Maximum M^2 ($\times 10^{-8}$)		
Initial	3.2 s^{-2}	33.9 s^{-2}
Spun-up	12.0 s^{-2}	50.0 s^{-2}
Maximum N^2 ($\times 10^{-4}$)		
Initial	1.5 s^{-2}	1.6 s^{-2}
Spun-up	3.1 s^{-2}	1.1 s^{-2}
Averaged mixed layer depth		
Initial	73 m	85 m
Spun-up	11 m	93 m

probability distribution function (PDF) of the density gradients measured by underwater gliders deployed around Station Papa over the period 2008–2010 (Pelland, 2018; Pelland et al., 2016). To reduce model spin-up time, density fronts are perturbed by a sinusoidal wave with a wavelength close to the first baroclinic deformation radius ($\lambda = 66$ km). Similar PSOM configurations were successfully used in previous studies (Mahadevan et al., 2012; Omand et al., 2015). The model does not simulate surface waves or boundary layer turbulence, but rather, examines the fate of particulate organic matter beneath the turbulent surface boundary layer.

Two main experiments are conducted using the same configuration of PSOM, where only initial conditions and surface forcing are varied: *Papa_summer* aims at generating ocean dynamics representing conditions in the Northeast Pacific in the summertime. Summer ocean dynamics are characterized by a flow generally in geostrophic balance, with relatively weak density gradients and low Rossby numbers ($Ro \ll 1$). *Papa_winter* aims at capturing wintertime ocean conditions in the region. A different dynamical regime is expected to dominate during wintertime when mixed layers are deeper and lateral density gradients enhanced, with sharper density fronts, filament-like features and localized Rossby number $Ro = \mathcal{O}(1)$ over spatial scales $\mathcal{O}(1$ km) (Callies et al., 2015; Mensa et al., 2013; Thompson et al., 2016). The individual characteristics of each of *Papa_summer* and *Papa_winter* are detailed below.

2.1.1. *Papa_summer* Model Experiment

In *Papa_summer*, PSOM is initialized based on climatological Argo data in April. The magnitude of the density gradient across the front is set to 3.34×10^{-6} kg/m^3/m, which corresponds to the 95th percentile of the PDF of density gradients measured in April from glider data collected in the region (Figure 2 and Table 1). The model is run with a timestep of 216 s and is allowed to spin-up for 60 days, allowing summer stratification to develop. The model is then run for 30 additional days, saving instantaneous model fields every 3 h for particle tracking. The month of April is chosen for initialization so the experiment would capture the onset of positive net heat fluxes, and the summer restratification that ensues in July–August (Figure 2). In this region, the summer stratification is associated with large primary productivity, particle production, and POC export (e.g., fecal pellets, dead phytoplankter; Plant et al., 2016).

2.1.2. *Papa_winter* Model Experiment

In *Papa_winter*, PSOM is initialized based on climatological Argo data in January. The frontal gradient is set to 3.54×10^{-5} kg/m^3/m, which corresponds to the 99th percentile of the PDF of density gradients measured in January from glider data collected in the region (Figure 3 and Table 1). The model is allowed to spin-up for 50 days allowing for the prescribed fronts to become unstable. To accommodate for the larger density gradients and stronger velocities, the advective timestep is shortened to 108 s and the horizontal diffusivity is lowered to 0.2 m^2/s throughout the experiment. The model is run for 30 additional days, saving instantaneous model fields every 1.5 h for particle tracking. The month of January is chosen for initialization so the experiment would capture the time of year where the mixed layer is the deepest, and Rossby number O (1) occur more frequently. The objective is for this experiment to contrast *Papa_summer* by capturing the statistics of ocean conditions dominated by submesoscale dynamics.

2.1.3. Validation

To ensure that PSOM simulations yielded realistic conditions for both *Papa_summer* and *Papa_winter*, distributions of horizontal (M^2) and vertical (N^2) buoyancy gradients are compared with glider observations collected over the period 2008–2009 (Pelland et al., 2016). During this period, underwater gliders sampled in a "bow-tie" pattern centered on Station Papa. Gliders sample the water column in a triangular wave

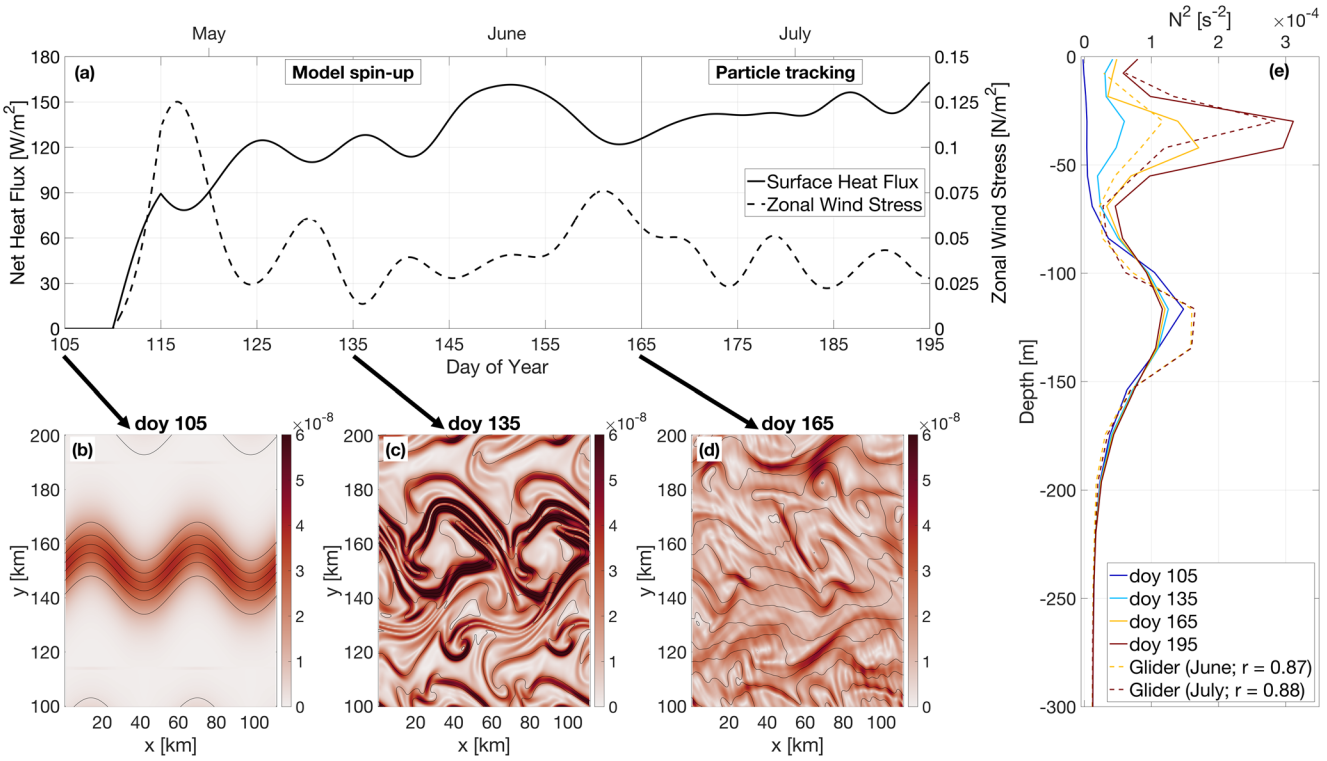

Figure 2. PSOM configuration for *Papa_summer*. (a) Time series of net heat fluxes and wind stress prescribed at the surface. Notice the positive heat fluxes, as well as downfront winds (i.e., eastward) persisting throughout the experiment. (b–d) surface horizontal buoyancy gradients $M^2 = |\nabla_H b|^2$ (in s^{-2}) at day of year (doy) 105, 135, and 165. Black contours show isopycnals (in kg/m^3; CI = 0.01 kg/m^3). (e) Vertical profile of the buoyancy frequency N^2 at day of year 105, 135, 165, and 195, showing the development of summer stratification centered at $z = 30$ m (solid lines). Monthly average vertical stratification obtained from glider profiles collected in June and July are superimposed (dashed lines), along with the correlation coefficient between observations and model outputs.

pattern, whose shape is easily affected by currents, due to the slow moving speed of the glider (~1 km/hr). It is therefore challenging to associate a specific spatial scale with gradients computed between glider profiles, as profile separation distances can be highly variable through depth and time. To circumvent this issue, horizontal buoyancy gradients are computed between each pair of glider profiles available within one branch of the bow-tie. Each along-track lateral buoyancy gradient is thus associated with a specific separation scale and a timestamp. Glider-based density gradients can be affected by internal waves. To filter the impact of internal waves on the PDF of horizontal buoyancy gradients, only gradients computed at a scale of twice the Rossby radius ±1 km are considered. Rossby radii are estimated from the glider data and are ~8 km in winter and ~20 km in summer.

2.2. Particle Tracking Experiments

2.2.1. Particle Advective Scheme

To quantify the impact of submesoscale dynamics on the export of particulate organic carbon (POC), Lagrangian particle trajectories are computed using the same scheme as in "TRACMASS" (Döös et al., 2013) with the flow fields from the two experiments described above. The three-dimensional, nondivergent velocity components from the faces of each C-grid cell are linearly interpolated onto the particle's position within the grid cell. For example, the eastward (along the x-axis) velocity of a particle is given by

$$u(x) = u_{i-1} + \frac{(x - x_{i-1})}{(x_i - x_{i-1})}(u_i - u_{i-1}), \tag{1}$$

where the subscripts $i - 1$ and i denote the western and eastern walls of the grid cell where the particle is located, respectively. This can be re-written as

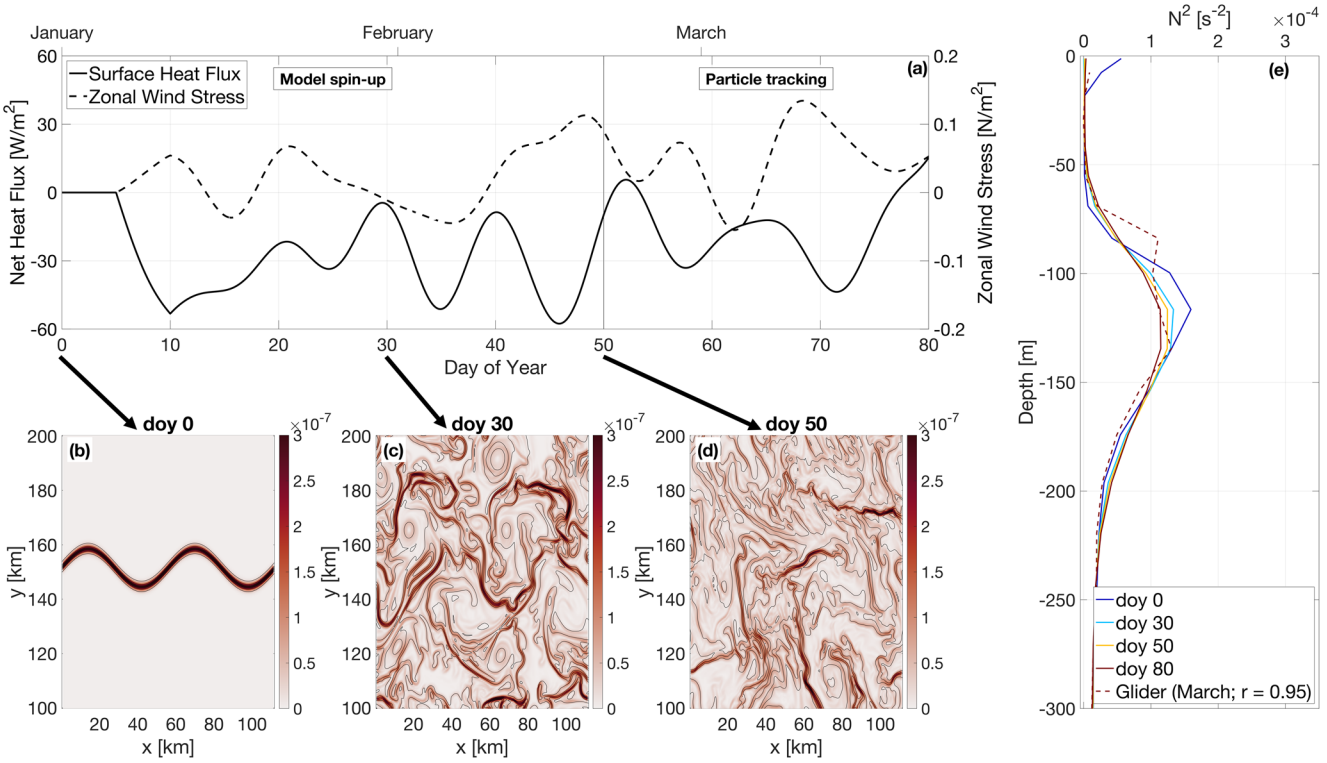

Figure 3. PSOM configuration for *Papa_winter*. (a) Time series of net heat fluxes and wind stress prescribed at the surface. Notice the mostly negative heat fluxes, as well as alternating zonal wind direction. (b–d) surface horizontal buoyancy gradients $M^2 = |\nabla_H b|^2$ (in s^{-2}) at day of year (doy) 0, 30, and 50. Black contours show isopycnals (in kg/m^3; CI = 0.01 kg/m^3). (e) Vertical profile of the buoyancy frequency N^2 at doy 0, 30, 50, and 80, showing the persistence of the halocline between $z = 80$ and $z = 180$ m throughout the experiment (solid lines). Monthly average vertical stratification obtained from glider profiles collected in March is superimposed (dashed line), along with the correlation coefficient between observations and model outputs.

$$\frac{\partial x}{\partial t} + \beta x + \delta = 0, \tag{2}$$

where $\beta = (u_i - u_{i-1})/\Delta x$ and $\delta = -u_{i-1} - \beta x_{i-1}$ (Döös et al., 2013). This differential equation can be solved analytically for $\beta \neq 0$ as

$$x_{t_1} = \left(x_0 + \frac{\delta}{\beta}\right)\exp^{-\beta(t_1 - t_0)} - \frac{\delta}{\beta} \tag{3}$$

the time it will take for the particle to reach the eastern or western face of the grid cell can be computed by taking $x_{t_1} = x_i$ or $x_{t_1} = x_{i-1}$, respectively, and solving for t_1. For each advective timestep, the times required for the particle to reach any of the six walls of the grid cell are computed using Equation 3. If any of those times is shorter than the advective timestep, the particle is advected until it reaches the cell wall. Then the flow field in the adjacent grid cell is considered and the particle is advected over the remaining time.

2.2.2. Particle Seeding

For all particle-tracking experiments, a single particle seeding event is prescribed. In the horizontal, particles are seeded every 250 m over the entire domain in the x-direction, and for $100 < y < 200$ km in the y-direction. The seeding is centered over the mean position of the central front (see Figure 2) and is therefore not affected by undesired effects created by the solid north-south solid boundaries. In the vertical, particles are seeded every 1 m between 75 and 85 m. This depth range is chosen as it corresponds to the average euphotic depth at Station Papa, defined by the 1% light level. Particle seeding is located at the base

of the euphotic layer where biological processes not captured by the particles (e.g., grazing, repackaging, aggregation, etc.,) are not as active (Ducklow et al., 2001). The euphotic depth was computed for the months of February and June over the period 2007–2016 from profiles of photosynthetically active radiation (PAR) collected at Station Papa as part of the long-term monitoring of Line P executed by the Department of Fisheries and Ocean Canada (https://www.waterproperties.ca/linep/index.php). The average euphotic depth computed for both of these months is around 80 m, which agrees with previously established estimates of the euphotic depth (Harrison et al., 2004; Sherry et al., 1999).

In each particle-tracking experiment, three different classes of particles are released. Each particle class is characterized by a different sinking velocity: 0.025, 1, and 5 m/day. In this study, these particle classes are referred to as slow-, intermediate-, and fast-sinking particles. This characterization is not based on the absolute value of the sinking rate, but rather on the ratio with vertical currents in the study region. The slowest-sinking class is essentially selected to represent nonsinking particles: based on the setup of our experiments, the slowest-sinking particles would take 400 days to sink 10 m through gravitational sinking, a timescale much greater than commonly observed remineralization timescales. While 5 m/day remains a relatively slow sinking rate, this "fast-sinking" velocity is chosen as an end-member velocity class of particle, based on the PDF of vertical velocities in the model. At any given time, at least 85% of the model vertical velocity is weaker than 5 m/day. The results presented for the 5 m/day sinking class can therefore be theoretically extrapolated to any class with a higher sinking velocity.

The advective timestep for particles is set to 1.5 h. The flow field is linearly interpolated in time between model outputs, justifying the higher temporal resolution used for particle tracking in *Papa_winter*. Particle positions are saved every 3 h, along with key model variables interpolated onto the particle positions (e.g., density, vorticity). Particles are tracked for four weeks (28 days). Each particle-tracking experiment contains 1,971,717 particles per sinking-velocity class, for a total of 9,858,585 particles.

2.2.3. Density and Biomass Spectra

To quantify vertical export fluxes, both the distribution of the number of particles and the associated biomass can be modeled based on two main variables: the particles' radii and the rate at which the number of particles changes with respect to the size. The particle number is modeled using a power-law function as a function of size that is driven by the paramater ξ. This slope ξ of the size spectrum of particles (also known as the Junge slope; White et al., 2015) is the slope of the log-log curve of particle number N versus particle radius r, where

$$N(r) = N_0\left(\frac{r}{r_0}\right)^{-\xi}. \tag{4}$$

Here, N_0 and r_0 represent a reference particle number and radius, chosen arbitrarily. Typical values for ξ derived from both in situ observations and satellite data have been reported to range from 3 to 6 (Kostadinov et al., 2009; White et al., 2015). For small particles (<400 μm) and relatively low temperature (<15°C), it has been shown that the relationship between particle radius r and sinking velocity w_s exhibits a range of variation and is difficult to determine empirically. Nevertheless, Stokes' law, where $w_s \propto r^2$, is often used as a lower-bound sinking velocity estimate (Bach et al., 2012).

Assuming a Stokes-like relationship, we can construct based on 4 a particle sinking velocity spectrum $N(w_s)$, as a function of the Junge slope ξ:

$$N(w_s) = N_0\left(\frac{w_s}{w_{s_0}}\right)^{-\xi/2}, \tag{5}$$

where w_{s_0} is the sinking speed of particles with radius r_0. For a specific slope and sinking-velocity class, an equivalent number of particles per simulated particle can be computed using Equation 5 (see Figure 4). For example, using the largest sinking velocity class as a reference (i.e., $w_{s_0} = 5$ m/day and $N_0 = 1{,}971{,}717$),

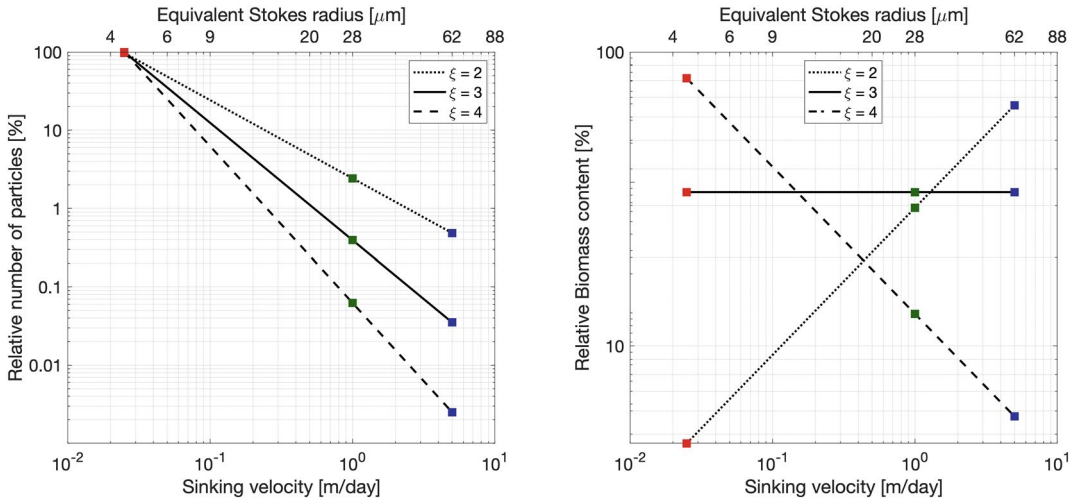

Figure 4. Relative number of particles (left) and biomass (right) as a function of sinking velocity w_s. Sinking velocity spectrum are shown for three different Junge slope ξ: 2 (dotted), 3 (solid), and 2 (dashed). Colored squares indicate the sinking velocities of the three particle classes modeled: 0.025 m/day (red), 1 m/day (green), and 5 m/day (blue).

and a spectral slope $\xi = 4$, each simulated particle with a sinking velocity of 0.025 m/day in fact represents 40,000 particles (Figure 4).

The relative biomass of a particle in a specific sinking-velocity class, $B_p(w_s)$ can be estimated if the biomass is assumed to scale with the particle's volume. The relative biomass of one particle in a sinking-velocity class w_s can therefore be computed as

$$B_p(w_s) = B_p(w_{s_0})\left(\frac{w_s}{w_{s_0}}\right)^{3/2} \tag{6}$$

where $B_p(w_{s_0})$ is the biomass of a particle in the sinking velocity class w_{s_0}. The total biomass associated with one simulated particle can be obtained by scaling (6) by the ratio $N(w_s)/N_0$:

$$B(w_s) = B_0\left(\frac{w_s}{w_{s_0}}\right)^{3/2}\frac{N(w_s)}{N_0} \tag{7}$$

where $B_0 = B_p(w_{s_0})$. Combining Equations 5 and 7 yields an expression relating the biomass associated with a simulated particle for a specific sinking-velocity class and the spectral slope (Figure 4):

$$B(w_s) = B_0\left(\frac{w_s}{w_{s_0}}\right)^{\frac{3-\xi}{2}}. \tag{8}$$

Using the same example as before where $\xi = 4$, if the amount of biomass associated with one simulated particle in the 5 m/day sinking-velocity class is taken as $B_0 = 1$, then one simulated particle sinking at 0.025 m/day contains 14.14 units of biomass and a single particle contains $14.14/40,000 = 3.5 \times 10^{-4}$ units of biomass (see Figure 4). This normalized formulation of particle number and biomass (see Equations 5 and 8) has the advantage that the impact of spectral slope on the relative export of biomass can be quantified without needing a large number of particle-tracking experiments, where the number of seeded particles would vary to account for the different spectral slopes. For the purpose of this study, only the relative amount of biomass is relevant. For simplicity, we define a normalized biomass unit for $\xi = 3$ as $B_0 = 1$. The values taken by B_0 for other Junge slopes ξ are computed under the condition that the total amount of biomass is kept constant (Figure 4b).

2.2.4. Particle Remineralization Scheme

Remineralization of particles as they sink through the water column impacts the amount of biomass exported. Slow-sinking particles generally contain less biomass and spend more time in the mixed layer, which means that they are remineralized at a shallower depth than faster sinking particles. Remineralization processes are complex, species-dependent, and generally not well-understood. In the absence of a consensus on a general functional form of particle remineralization, we rely on an idealized relationship which assumes that the biomass content of a particle decreases in time proportionally to the particle volume. Remineralization is thus modeled as an exponential decrease of biomass with time at a rate k (Iversen & Ploug, 2010, 2013)

$$B(t) = B^0 \exp(-kt), \tag{9}$$

where B^0 denotes the biomass content at $t = 0$ days, and the remineralization rate is taken to be $k = 0.13$ day^{-1} in this study (Iversen & Ploug, 2010). This remineralization rate is independent of particle sinking velocity, and seems to lie within the range of other estimates (Ploug et al., 2008; Iversen & Ploug, 2010, 2013). The change in biomass with time is in turn expected to affect the sinking velocity of the particle. Given that $B \propto w^{3/2}$ (see Equation 6), particles in all sinking-velocity classes undergo a decay in sinking speed according to

$$w_s(t) = w_s^0 \exp\left(-\frac{2kt}{3}\right), \tag{10}$$

where w_s^0 is the initial sinking velocity at $t = 0$ days. In this study, the impact of remineralization is thus considered through the implementation of a time-dependent sinking velocity (Equation 10). While particles classes are classified based on their initial sinking-velocity, it is worth noting that over the length of the particle-tracking experiments that include remineralization (28 days), particle sinking speeds slow down to 10% of their initial velocity.

3. Results

3.1. Seasonally Varying Dynamical Regimes

Two model experiments are designed to capture different dynamical conditions observed in the Northeast Pacific Ocean in summer and winter. *Papa_summer* is initialized in early spring (doy 105) when the water column is characterized by a relatively deep mixed layer (~100 m) and a halocline located between 100 and 150 m (Figure 2). The forcing by a realistic, positive, net heat flux generates the restratification of the water column, with the development of a strong thermocline between 25 and 50 m leading to the shoaling of the mixed layer and a subsurface peak in N^2 at about 30 m (see Figure 2). A comparison between model outputs and monthly averaged density profiles from underwater gliders collected in June and July over the period 2008–2009 yields correlation coefficients of $r = 0.87$ and $r = 0.88$, respectively. These high correlations suggest that *Papa_summer* numerical experiment captures the vertical spring and summer conditions in the Northeast Pacific Ocean.

In the horizontal, the prescribed density fronts progressively become unstable within the first 60 days of the experiment (Figure 2). During this time, the Total Kinetic Energy (KE_{tot}) contained in the model domain slowly increases before reaching a maximum at doy 162, where it remains relatively constant for the rest of the simulation. The flattening of the KE_{tot} curve is used to determine the time necessary for the simulation to spin-up, hence determining the start day of the particle-tracking experiments. The ocean dynamics associated with *Papa_summer* are characterized using PDFs of horizontal buoyancy gradients ($M^2 = |\nabla_H b|^2$), vertical velocities (w), and Rossby numbers computed from the normalized vertical component of the relative vorticity ($Ro = (v_x - u_y)/f$ where $f = 1.12 \times 10^{-4}$; Figure 5).

Lateral buoyancy gradients in the summer are relatively weak $\mathcal{O}(10^{-8}$ s$^{-2})$ and result in low Rossby numbers $\mathcal{O}(0.1)$, with positive relative vorticity on the denser (north) side of the front and negative relative vorticity on the lighter (south) side of the front. Corresponding vertical velocities are consistently weaker than 1 m/day ($<10^{-5}$ m/s) and are characterized by regions of weak upwelling and downwelling on 10 km scales,

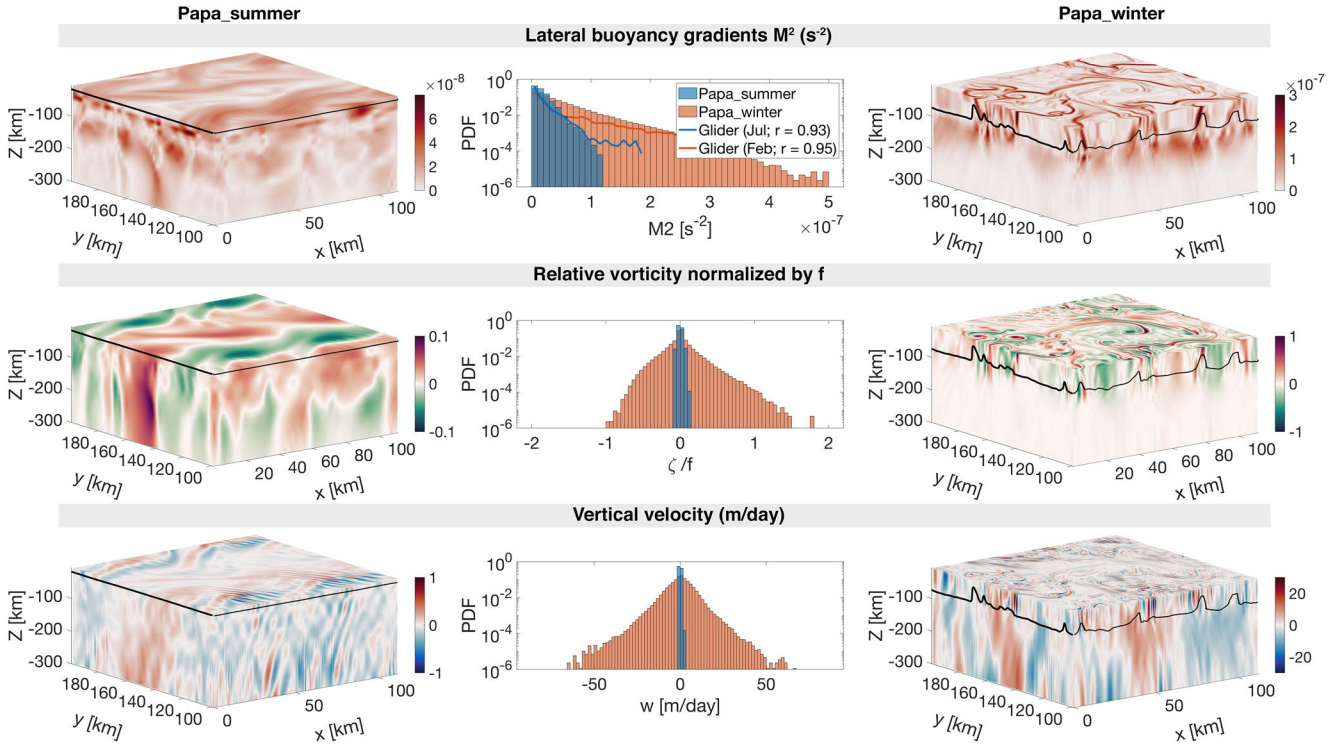

Figure 5. Snapshots of M^2 (top), ζ/f (middle), and w (bottom) half-way through the particle tracking experiment for *Papa_summer* (left) and *Papa_winter* (right), with the Mixed Layer Depth indicated by the solid black line. The corresponding probability distribution functions (PDFs) are shown in the center for both *Papa_summer* (blue) and *Papa_winter* (red). Note the different colorbars used for *Papa_summer* and *Papa_winter*. Histograms of M^2 computed from glider data at Station Papa in February (blue line) and July (red line) are superimposed in the top middle panel.

associated with the meandering of the front (Bower & Rossby, 1989). Alternating bands of upwelling and downwelling at $\mathcal{O}$(1 km) spatial scale are superimposed, and likely caused by propagating internal waves. Coherent vertical velocities structures extend to depths much greater than the mixed layer depth (~25 m; Figure 5). The amplitude of the vertical velocity field coincides with the expected order of magnitude given by the scaling $w \propto RofU/N$ (Mahadevan, 2016): using $Ro \sim 0.1$ (Figure 5), $n \sim 10^{-2}$ s^{-1} (Figure 2), $f \sim 10^{-5}$ s^{-1}, and $U \sim 0.01$ m/s, we obtain $w \sim 10^{-6}$ m/s, or $\sim 10^{-1}$ m/day.

Papa_winter is, on the other hand, initialized in the winter (doy 0) to capture a time period where the mixed layer depth is deeper (~100 m) and density gradients more pronounced (Pelland et al., 2016). At this time of year, the water column in this region is characterized by the presence of a deep halocline between 100 and 150 m (Figure 3, Pelland et al., 2016). After spin-up, the vertical stratification remains consistent throughout the model run, and compares well with the vertical profile obtained from glider observations for the month of March ($r = 0.95$; see Figure 3). In the horizontal, prescribed density fronts are much sharper than in summer (i.e., over smaller spatial scales O [1 km] vs. O [10 km]). Because of these stronger density gradients, combined with the alternating zonal winds and constantly negative surface heat flux, the fronts become unstable more rapidly than in summer (Figure 3). As a result, KE_{tot} starts to plateau at doy 48. The experiment is considered spun-up by doy 50 and the particle-tracking experiment is initialized.

The frontal structures visible in the horizontal buoyancy gradient field are associated with filaments of relatively high Rossby number of $\mathcal{O}$(1) (Figure 5). The PDF of relative vorticity reveals a positively skewed distribution ($s = 0.68$). This is in agreement with the fact that the relative vorticity is more likely to be cyclonic than anticyclonic, based on conservation of potential vorticity (Hoskins & Bretherton, 1972). Regions with high Rossby number are localized and located in the mixed layer exclusively. In places where the local Rossby number reaches $\mathcal{O}$(1), geostrophic balance is lost and a vertical secondary ageostrophic circulation begins to slump the isopycnals and restore the flow to a more geostrophically balanced flow.

This ageostrophic secondary circulation therefore generates "hot spots" of higher vertical velocities. The fine-scale structures in the vertical velocity field corresponding to $\mathcal{O}(1)$ Rossby numbers can be seen in Figure 5, with local vertical velocities up to 60 m/day ($\sim 7 \times 10^{-4}$ m/s). Contrary to the PDF of relative vorticity, the distribution of vertical velocities demonstrate a negative skewness ($s = -0.25$). This is in agreement with the theory: In fact, positive relative vorticity is associated with the dense side of a density front, where vertical velocities are negative (Mahadevan, 2016). Once again, the amplitude of these vertical velocity hot spots is coherent with the scaling $w \propto RofU/N$: using $Ro \sim 1$, $N \sim 10^{-2}$ 1/s, $f \sim 10^{-5}$ 1/s, and $U \sim 0.1$ m/s, we obtain $w \sim 10^{-4}$ m/s, or $\sim 10^{1}$ m/day.

Comparing *Papa_summer* and *Papa_winter* highlights the different dynamical regimes in the two experiments. In *Papa_winter*, density fronts tend to be sharper, meaning larger density gradients over shorter spatial scales. When computed at the kilometer-scale, the PDF of horizontal buoyancy gradients in *Papa_winter* exhibits a longer tail than in *Papa_summer* (Figure 5). When compared to observations, the PDFs of M^2 in *Papa_summer* and *Papa_winter* demonstrate a correlation with observations of $r = 0.93$ and $r = 0.95$, respectively.

The wider PDF of vertical velocities in *Papa_winter* shows advective velocities that match and exceed typical gravitational sinking velocities, particularly for smaller, and therefore slower-sinking, particulate organic material. The secondary ageostrophic circulation that develops at submesoscales (i.e., Ro O (1)) therefore generates an export mechanism that directly competes with the traditional paradigm that relies on gravitational sinking leading the export of particulate matter in the ocean.

3.2. Gravitational and Advective Export of POC

Both model experiments described above were then used to investigate the relationship between ocean dynamics and particle downward flux, using Lagrangian particle-tracking. Domain-averaged, downward particle flux is expected to be a combination of the flux driving by gravitational sinking ($\langle w_s B \rangle$), and by the vertical advective currents affecting the particle along its pathway ($\langle wB \rangle$). The deviation in particle depths from the traditional one-dimensional gravitationally driven model is shown in Figure 6 for both summer and winter cases. In the summer, the PDF of particle density versus depth remains relatively narrow through time, and is centered on a depth level that can be predicted using a simple one-dimensional gravitational model (see shaded curves in Figure 6). The spread in the particle density also vary little among particle classes with different sinking velocities, suggesting that downward fluxes of particles is greatly dominated by gravitational settling and is not subject to significant vertical ocean currents.

In the winter, however, PDFs of particle density versus depth is wider, in agreement with the stronger vertical ocean currents occurring in the winter (see Figure 5). A top-view of the deviation in the downward particle flux from the traditionally considered one-dimensional gravitational model can be seen in Figures 6a–6c. Slower-sinking particles deviate more than faster-sinking particles, exhibiting median depth anomalies up to 50 m. This is due to the fact that slower-sinking particles spend more time in the mixed layer, where most of the stronger vertical currents tend to occur (Figure 5). An interesting result emerges from the spatial distribution of the depth-anomaly: both positive (i.e., particles are shallower than expected) and negative (i.e., particles are deeper than expected) anomalies are organized into features with a length-scale $\mathcal{O}$(1–10 km). This further highlights the importance of winter submesoscale circulation for vertical fluxes of particles.

A relative amount of biomass is associated to the particles using Equation 8. PDFs of relative biomass as a function of the vertical velocity is shown in Figure 7. Following the traditional paradigm derived from the simple one-dimensional gravitational model, the downward flux of biomass in the summer is dominated by faster-sinking particle classes capable of carrying particulate material downwards more efficiently. The contribution of slower-sinking particles, however, depends critically on the slope of the size spectrum (see Figure 4). As the Junge slope increases, the spectrum of biomass steepens, and the relative contribution of slower-sinking particles to the downward biomass flux significantly increases (Figure 7c). In fact, the contribution of slower-sinking particles to the summer downward flux increases by a factor 100 (from 0.2% to 20%) when the Junge slope varies from $\xi = 2$ to $\xi = 4$. While significant, the impact of a change in the

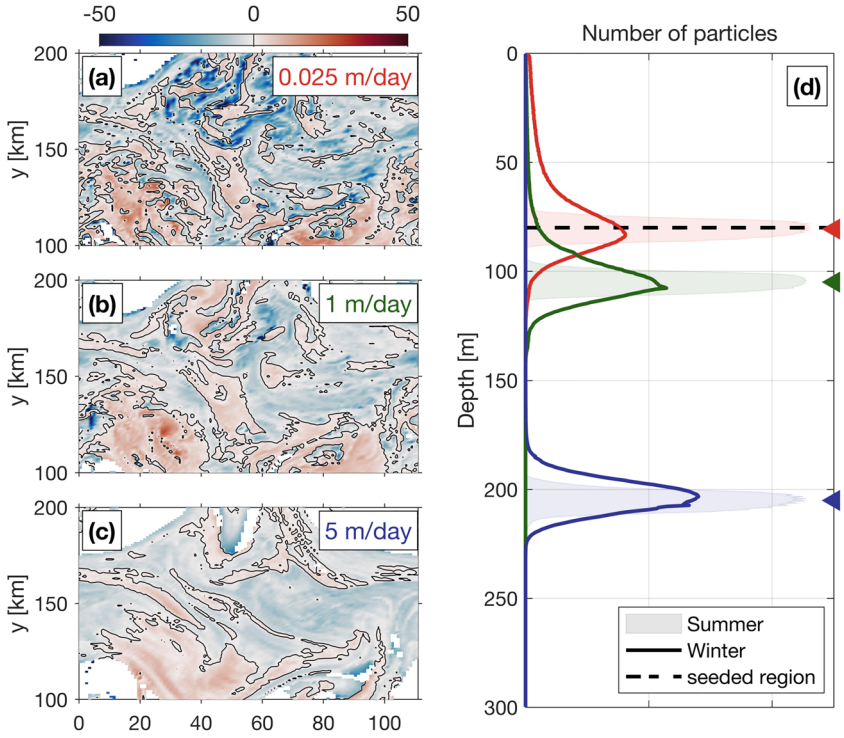

Figure 6. (Left) The median depth anomaly of particles with a sinking speed (a) 0.025 m/d, (b) 1 m/d, (c) 5 m/d within each grid cell for the winter case 25 days after particles are released. The "depth anomaly" is with respect to the "expected" sinking depth (= sinking speed × time since release). Blue (red) grid cells indicate that the median depth of particles in this cell is deeper (shallower) than expected, based on a one-dimensional gravitational model where $z = w_s \times t$ (right) (d) probability distribution function (PDF) of particles as a function of depth for each velocity class (red = 0.025 m/day; green = 1 m/day; blue = 5 m/day). The winter distribution is shown as thick lines, while the summer distribution is represented by the shaded regions. Triangle markers indicate the expected depth of particles after 25 days based on the one-dimensional gravitational model, which is used as a reference to compute the depth anomalies. Release depth is indicated by the thick dashed line.

Junge slope in summer conditions does not challenge the dominant role played by faster-sinking particles. This result can be explained by the fact that, in the summer, vertical velocities are weak and vertical biomass fluxes are therefore gravitationally driven ($\langle w_s B \rangle > \langle wB \rangle$).

In the winter, PDFs of relative biomass as a function of vertical velocities present a much larger spread, with velocity magnitudes exceeding 50 m/day. For $\xi = 2$, the relative contribution of slower-sinking particles to the downward flux significantly increases from 0.2% in the summer to about 3% in the winter, demonstrating the impact advective velocities alone can have on vertical fluxes (Figure 7b). Nevertheless, slower-sinking particles remain a relatively small contributor to the total downward flux of biomass. When winter ocean dynamics are coupled with a steeper Junge slope, however, slower-sinking particles largely dominate the downward biomass flux. In our winter simulations with $\xi = 4$, we find that the slowest-sinking particle class is responsible for about 79% of the biomass flux (Figure 7d).

Our results show that both a steepening of the particle size spectrum and the presence of submesoscale dynamics can enhance the contribution of slower-sinking particles to the downward biomass flux. While the former is simply due to an increase in particle density in slower-sinking particle classes, the latter is attributed to the larger vertical velocity generated by submesoscale instabilities. When both are combined, as expected in the wintertime, slower-sinking particles then become the leading contributor to the downward biomass transport. However, slower-sinking particles are generally expected to remineralize on timescales shorter than their export timescale, fueling the argument that the focus should be upon faster-sinking particle classes. The impacts of remineralization on export are thus considered in the following section to test the robustness of the findings.

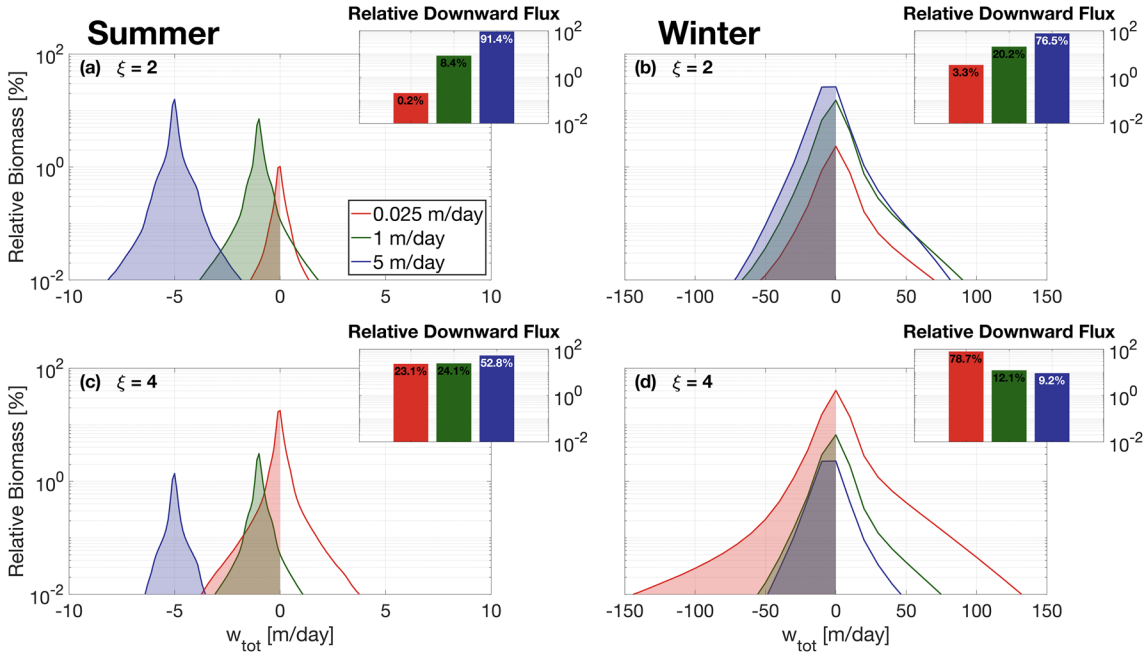

Figure 7. Probability distribution function (PDF) of relative biomass versus total vertical velocity (sinking + advective) along particle trajectories in the summer case (left) and winter case (right), with a Junge slope of 2 (top) and 4 (bottom). PDFs are computed from the whole 24-day particle tracking experiments. Inserts show the integrated relative downward biomass flux associated with each sinking-velocity class, categorized according to their initial sinking velocity (red = 0.025 m/day; green = 1 m/day; blue = 5 m/day). Both winter dynamics and steeper Junge slopes tend to increase the relative contribution of slower-sinking particles.

3.3. Particle Remineralization

Both submesoscale dynamics and the Junge slope were identified as key factors impacting the respective role played by different particle classes in driving downward biomass fluxes. Simple Lagrangian particles were used to isolate the effects of these two factors. In reality, however, sinking velocities of particulate matter varies in time as the particles slowly remineralize. A remineralizing behavior was therefore implemented for the Lagrangian particles, using Equation 10, to investigate the impact that remineralization processes have on our findings. The traditional paradigm relies on the fact that slow-sinking particles tend to fully remineralize over short timescales, further enhancing the importance of faster-sinking particles classes in driving downward biomass fluxes. While this paradigm holds for flatter Junge slope, where the biomass content is dominated by faster-sinking particles, it becomes unfit at steeper slopes.

Figure 8 compares the relative biomass and downward biomass fluxes associated with each of the modeled particle classes for $\xi = 2$ and $\xi = 4$ including the remineralization scheme. As previously detailed, downward fluxes of biomass are dominated by faster-sinking particles during summertime and in the absence of remineralization (see Figure 7). This is due to the fact that the flux of biomass $\langle w_{tot} B \rangle = \langle w_s B \rangle + \langle wB \rangle$ is driven by $\langle w_s B \rangle$, despite a smaller relative biomass content per particle. This is characteristic of a gravitationally driven system, where settling velocity dictates the contribution to downward fluxes. Implementing remineralization processes, however, directly affects the particle settling velocity which slows down as particles remineralize. This effect can particularly be seen in Figures 8a and 8c, where PDFs of relative biomass per particle class are shifted toward weaker vertical velocities than in the absence of remineralization, as predicted by Equation 10.

In a advectively driven system where $\langle w_s B \rangle \sim \langle wB \rangle$, the relative amount of biomass content in a particle class becomes important and dictates the respective contribution of each particle class to the total downward biomass fluxes. This shift from a gravitationally driven to an advectively driven system is observed when implementing particle remineralization in the summer (Figure 8): in the absence of remineralization, faster-sinking particles dominate the downward biomass fluxes (53%; see Figure 7c). When remineralization

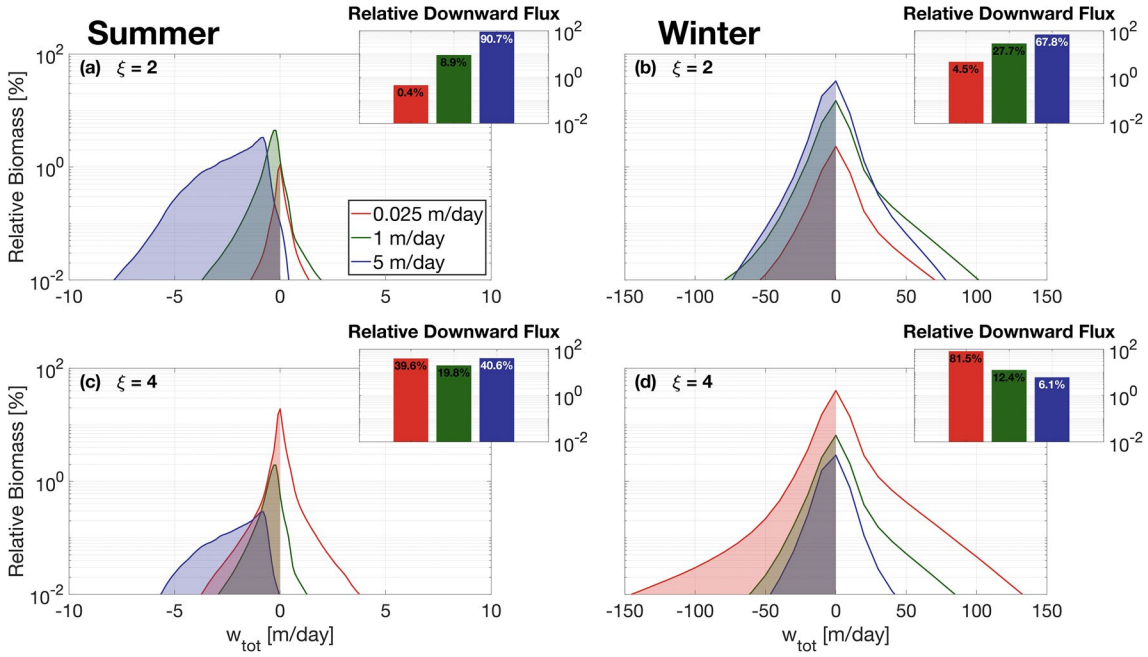

Figure 8. Same as Figure 7, but including particle remineralization (see Equation 10).

processes are considered, slower-sinking particles contribute more to biomass fluxes (see inset in Figure 8c). As shown in Figure 7, downward biomass fluxes in the wintertime are generally advectively driven, due to the larger vertical velocities associated with wintertime ocean dynamics. Biomass fluxes are dominated by the slower-sinking particles when $\xi = 4$, representing 79% of the downward biomass flux (Figure 7d). Even after implementing the remineralization scheme, slower-sinking particles remain the largest contributor to downward biomass fluxes (82%; see Figure 8d).

These results highlight the importance in considering slower-sinking particle classes when considering downward biomass fluxes. It also demonstrates that, contrarily to the traditional paradigm, remineralization processes enhance the role played by slower-sinking particles in biomass fluxes, in cases where the biomass spectrum slope is negative.

4. Discussion

4.1. Dynamical Regimes

Papa_summer and *Papa_winter* experiments were designed to statistically capture the ocean dynamics at Station Papa (145°W, 50°N) in the Northeast Pacific Ocean. After spin-up, the model demonstrated similar distributions of both horizontal (M^2) and vertical (N^2) density gradients to observational estimates from underwater gliders (see Figures 2, 3, and 5). The two experiments, however, show significantly different distributions of M^2, with the winter distribution exhibiting a longer tail, due to sharper density gradients. The tail of the wintertime distribution is only partially captured by the glider data, due to the fact that underwater gliders sampled gradients at spatial scales of 10 km and greater, while the model has a horizontal resolution of 500 m, allowing sharper submesoscale fronts and filaments to be formed.

Studies investigating submesoscale dynamics traditionally focused on regions where the presence of submesoscale fronts and filaments are established, such as western boundary currents with strong gradients (D'Asaro et al., 2011; Thomas, Tandon, & Mahadevan, 2013), or the edge of mesoscale features (van Haren et al., 2006; Waite et al., 2016). The seasonality in submesoscale dynamics captured in the glider data set at Station Papa and reflected in the model experiments, echoes the behavior seen from recent observational studies conducted at a similar latitude in the Atlantic Ocean, which demonstrate the intensification of submesoscale dynamics in the wintertime (Buckingham et al., 2016; Erickson & Thompson, 2018; Thompson

et al., 2016). Despite being sometimes qualified as an "eddy desert" with low kinetic energy (Chelton et al., 2011), ocean characteristics in the eastern part of the Pacific subpolar gyre suggest the presence of submesoscale features in the wintertime: strong density gradients, localized Rossby numbers of order 1, a balanced Richardson number $Ri_b = \frac{f^2 N^2}{M^4}$ smaller than 1, a positively skewed distribution in vorticity, and a negatively skewed distribution of vertical velocities (see Figure 5; Buckingham et al., 2016; Thomas, Taylor, et al., 2013; Rudnick, 2001).

Strong downward velocities are hypothesized to enhance POC export by advecting slower-sinking particles out of the mixed layer. *Papa_winter* indeed exhibits vertical velocities more than 20 times larger than in *Papa_summer*. The vertical currents in *Papa_winter*, however, tend to be much patchier than the weaker vertical currents observed in *Papa_summer*. Because both particle production and downward vertical velocities present a high degree of patchiness, it requires a certain level of covariance between the two fields for the export to effectively be enhanced (Mahadevan et al., 2012). A more realistic seeding strategy for Lagrangian particles, such as one guided by biological tracers, would likely provide important information toward a better understanding of the effects of patchiness on POC export at submesoscales

The hypothesis tested in this study is that submesoscale activity enhances export of particulate matter at Station Papa by shortening the export timescale of particulate matter. The wintertime intensification in submesoscale activity has the potential to indeed enhance export (see discussion in Section 4.2). However, the seasonal cycle in submesoscale activity is out of phase with the one in net community productivity, which peaks in the spring and summertime when the mixed layer is shallower (Plant et al., 2016). Two mechanisms are therefore present to potentially sustain a year-long POC export flux: In the winter, less particulate material is present in the mixed layer, but active submesoscale dynamics tend to enhance the POC export flux by advecting the more numerous slower-sinking particles into the ocean interior. In the summer, the production of POC is at its yearly maximum, but export tends to be dominated by gravitational sinking, which favors faster-sinking particles and thus exclude part of the particle spectrum from contributing to the export flux.

4.2. Downward Fluxes

Analyses of particle tracking experiments reveal that the contribution of slower-sinking particles to the downward particulate flux depends on two main factors: (1) the dynamics of the oceanic flow field, and (2) the slope of the size spectrum (i.e., the Junge slope ξ).

Mixed layer ocean dynamics at station Papa change significantly between the winter and the summer. In the winter, submesoscale dynamics are intensified, and sharp fronts and filaments develop in the mixed layer. This seasonal change in dynamics is consistent with recent observations (Buckingham et al., 2016; Thompson et al., 2016), and models (Brannigan et al., 2015; Callies et al., 2015; Rocha et al., 2016) characterizing the seasonal cycle of submesoscale dynamics. The winter intensification in submesoscale dynamics was proven to have an important impact on the downward flux of all sinking-velocity classes modeled in this experiment.

In the summer, gravitational sinking governs a downward particulate flux, which is dominated by faster-sinking particles, with little to no contribution from slower-sinking particles. In the winter, however, vertical fluxes tend to be advectively driven, which leads to a slightly weaker downward flux of faster-sinking particles than in the summer due to resuspension, but a much larger flux of slower-sinking particles, which are present in far greater numbers (Figure 7). The gravitationally driven flux in the summer is mechanistically different from the advectively driven winter flux, which raises the question as to which process is most efficient in driving a downward flux of particulate material.

In the absence of remineralization, both a steeper size spectrum slope ($\xi > 3$ in this case) and enhanced submesoscale dynamics, increase the contribution of slower-sinking particle classes to the downward biomass flux. This is only when both of these conditions are combined, however, that slower-sinking particles dominate the downward flux of biomass (Figure 7). This is a significant result, as Junge slopes greater than three have been observed in the ocean: In situ observations yield average spectral slopes varying between 3.5 and 4.5 (see Table 2 in Kostadinov et al., 2009), while spectral analysis of satellite data suggest global

spectral slopes varying between 3 and 6. More recent observational work located in the Northeast Pacific, including Station Papa, found a spectral slope also greater than 3 (Cram et al., 2018; White et al., 2015). Junge slopes are expected to vary in space, depending on the community composition, both lateraly and vertically (Kostadinov et al., 2009; White et al., 2015), as well as in time; spectrum slopes tend to be flatter during a spring bloom event, where larger particles (e.g., diatoms) are produced in large quantities, and steeper during the wintertime, when communities are mostly composed of small particles (Behrenfeld, 2010; Dale et al., 1999; Parsons & Lalli, 1988). The threshold value of $\xi = 3$ for a change in the biomass spectral slope (see Figure 4b) is of course a consequence of first-order approximations used in this study describing the relationships between particle size, sinking velocity, and biomass content. Nevertheless, our results demonstrate the importance of including the smaller particle size range of the particle spectrum, in the estimation or measurement of vertical fluxes, especially when submesoscale dynamics are active. It also highlights the importance of better constraining the relationships linking particle size, sinking velocity, and biomass content.

Introducing remineralization processes significantly decreases the biomass flux. Counter-intuitively, however, the implementation of a remineralization scheme further strengthens the contribution of slower-sinking particles to the biomass flux, once particles have left the euphotic layer (Figure 8). This can be explained by the fact that remineralization processes have a greater impact on sinking-velocity classes that rely on gravitational sinking to be exported, as these particles decelerate as they remineralize. In the summer, all particle classes are similarly affected by remineralization, as downward fluxes are gravitationally driven. In the winter, however, slower-sinking particles are exported through advective processes. Their export timescale is barely affected by remineralization processes as it only depends on local ocean dynamics. Changing the remineralization timescale would therefore only affect the results in a gravitationally driven flux: increasing the timescales (i.e., slower remineralization) would give more weight to the smaller classes, while decreasing the timescales (i.e., faster remineralization) would favor faster sinking particles to drive the downward flux. In an advectively driven flux, however, all particles classes are equally affected by remineralization (i.e., lose 12% of their biomass per day). While this affects the total amount of biomass flux, it does not impact the respective contributions of the different particle classes to the downward biomass flux.

These results are robust to the range of sinking rates explored. If one considers a particle class with a sinking rate far exceeding the vertical advective velocity (e.g., 100 m/day; Turner, 2015), then the associated biomass flux can be estimated by relying on the traditional one-dimensional paradigm, assuming $w_{tot} \approx w_s$. Combining this approximation with Equation 8 shows that the slope of the biomass flux spectrum is positive for $\xi < 5$, in which case very fast-sinking particles would dominate vertical biomass fluxes. However, for $\xi > 5$, the slope of the biomass flux spectrum becomes negative as well, meaning that the biomass flux is always dominated by the slow-sinking particle classes, regardless of the ocean dynamical regime. While values of $\xi > 5$ have been estimated by Kostadinov et al. (2009) using satellite data, in situ estimated values of ξ tend to range between 2 and 4.5 (Cram et al., 2018; White et al., 2015).

Our findings add to a rapidly growing body of literature supporting the key role of an export pathway from the upper ocean to the interior driven by vertical ocean dynamic, and directly affecting particulate carbon. This pathway is often referred to as the "particle-injection pump" (Boyd et al., 2019), or "subduction hot spots" (Levy et al., 2013; Omand et al., 2015; Resplandy et al., 2019), and is consistently identified as an important mechanism to POC export (Llort et al., 2018; Siegel et al., 2016; Stukel et al., 2017, 2018). Vertical mixing at submesocales, in fact, was found to be equally important for the subduction of tracers from the mixed layer to the interior, and the obduction of tracers having a subsurface maximum (e.g., nutrients) (Mahadevan, 2016; Taylor et al., 2020). The importance of the seasonality in submesoscales dynamics highlighted in our process-oriented study supports recent findings obtained from high-resolution observations: Both Erickson and Thompson (2018) and Bol et al. (2018) studied glider data to conclude that the winter intensification of submesoscale dynamics can generate a large downward export of POC. The third key component to our results, additionally to the roles of submesocale dynamics and seasonality, is the contribution of smaller, slower-sinking POC to the export flux. The results presented in this work directly align with studies providing evidence that smaller particles contribute significantly to the POC flux (Baker et al., 2017; Bol et al., 2018; Riley et al., 2012; Taylor et al., 2020). The magnitude of the downward flux driven by slow-sinking particles, however, is still uncertain and was sometimes estimated to be largely compensated by an

upward flux (Resplandy et al., 2019), indicating a possible dependence on data resolution. In our study, we piece together three key components to POC vertical fluxes to characterize limit cases where ocean conditions favor either a gravitationally or advectively driven POC flux. We reached the conclusion that slow- and nonsinking particles, compared to the magnitude of vertical currents, should be considered when studying the downward flux of particulate matter in the upper ocean. Furthermore, the patchiness associated with both particle production and submesoscale features poses a real observational challenge to properly resolve vertical fluxes. Based on our findings, subsequent studies could focus on testing the impact of patchiness on vertical fluxes. In the wintertime, when size spectral slope is steep and submesoscale dynamics most active, vertical fluxes could be grossly underestimated depending on the level of co-occurrence between particle production and stronger vertical currents.

5. Conclusion

The main conclusions of this study are:

1. Ocean dynamics in the subpolar Northeast Pacific exhibit a seasonal cycle with low submesoscale activity in the summertime, and more submesoscale features present in the wintertime. Submesoscale dynamics generate larger, and asymmetric, vertical currents leading to a vertical biomass flux driven by advective processes, as opposed to gravitational sinking in the summertime
2. Submesoscale dynamics generally enhance the downward particulate flux by increasing the contribution of slower-sinking particles to the total flux through advective transport. The slower-sinking particles are found to be significant for export, and can be even make the dominant contribution under certain conditions
3. The contribution of slower-sinking particles to the downward biomass flux depends on the slope of the particle size spectra (i.e., the Junge Slope), that controls the relative number of particles per size class. Two cases emerge from this study

(a) If the Junge slope is smaller than 3, larger particles contribute most to vertical biomass fluxes independently of flow dynamics, as there are no mechanisms capable of selectively advecting slower-sinking particles. The system is described as gravitationally driven.

(b) If the Junge slope is greater than 3, as most commonly observed, ocean dynamics become key for determining which particle classes dominate the downward flux. As submesoscale dynamics become more active, ageostrophic circulations leading to larger vertical velocities develop. In these conditions, downward biomass fluxes are largely driven by the slower-sinking particle classes.

4. Remineralization processes below the euphotic depth logically reduce the amount of biomass flux. However, it unexpectedly enhances the role of slower-sinking particles, which are advectively transported. The impact of remineralization below the euphotic depth is greater on faster-sinking particles since it affects both the biomass content and their sinking velocity

Data Availability Statement

All data used in this manuscript are publicly available: Ocean Station Papa data are available on PMEL's website (https://www.pmel.noaa.gov/ocs/Papa; PMEL, 2018) and gridded Argo products can be downloaded at http://www.seanoe.org/data/00348/45945 (Gaillard, 2015). Glider data is archived at the University of Washington's Library (http://hdl.handle.net/1773/41,656; Pelland, 2018). Both the code and data set necessary to reproduce analysis and figures are publicly available (Dever, 2020a, 2020b). Finally, authors are grateful to the two anonymous reviewers for their valuable comments and suggestions.

Acknowledgments
The work was funded by NASA grant NNX16AR48 G, to complement the EXport Processes in the global Ocean from RemoTe Sensing (EXPORTS) program. The authors would like to thank A. Thompson (Caltech) for his useful comments and suggestions, N. Pelland (NOAA) and C. Eriksen (University of Washington) for sharing the glider data collected at Ocean Station Papa, as well as S. Essink for his assistance in developing the particle-tracking code.

References

Alkire, M., D'Asaro, E., Lee, C., Perry, M., Gray, A., Cetinic, I., et al. (2012). Estimates of net community production and export using high-resolution, Lagrangian measurements of O_2, NO_3^-, and POC through the evolution of a spring diatom bloom in the North Atlantic. *Deep-Sea Research I*, *64*, 157–174. https://doi.org/10.1016/j.dsr.2012.01.012

Armstrong, R. A., Lee, C., Hedges, J. I., Honjo, S., & Wakeham, S. G. (2001). A new, mechanistic model for organic carbon fluxes in the ocean based on the quantitative association of POC with ballast minerals. *Deep Sea Research Part II*, *49*(1), 219–236. https://doi.org/10.1016/S0967-0645(01)00101-1

Bach, L. T., Riebesell, U., Sett, S., Febiri, S., Rzepka, P., & Schulz, K. G. (2012). An approach for particle sinking velocity measurements in the 3–400 μm size range and considerations on the effect of temperature on sinking rates. *Marine Biology*, *159*(8), 1853–1864. https://doi.org/10.1007/s00227-012-1945-2

Baker, C. A., Henson, S. A., Cavan, E. L., Giering, S. L., Yool, A., Gehlen, M., et al. (2017). Slow-sinking particulate organic carbon in the Atlantic Ocean: Magnitude, flux, and potential controls. *Global Biogeochemical Cycles*, *31*(7), 1051–1065. https://doi.org/10.1002/2017GB005638

Behrenfeld, M. J. (2010). Abandoning sverdrup's critical depth hypothesis on phytoplankton blooms. *Ecology*, *91*(4), 977–989. https://doi.org/10.1890/09-1207.1

Bol, R., Henson, S. A., Rumyantseva, A., & Briggs, N. (2018). High-frequency variability of small-particle carbon export flux in the Northeast Atlantic. *Global Biogeochemical Cycles*, *32*(12), 1803–1814. https://doi.org/10.1029/2018GB005963

Bower, A. S., & Rossby, T. (1989). Evidence of cross-frontal exchange processes in the gulf stream based on isopycnal RAFOS float data. *Journal of Physical Oceanography*, *19*(9), 1177–1190. https://doi.org/10.1175/1520-0485(1989)019⟨1177:EOCFEP⟩2.0.CO;2

Boyd, P. W., Claustre, H., Levy, M., Siegel, D. A., & Weber, T. (2019). Multi-faceted particle pumps drive carbon sequestration in the ocean. *Nature*, *568*(7752), 327–335. https://doi.org/10.1038/s41586-019-1098-2

Brannigan, L., Marshall, D. P., Naveira-Garabato, A., & George Nurser, A. (2015). The seasonal cycle of submesoscale flows. *Ocean Modelling*, *92*, 69–84. https://doi.org/10.1016/j.ocemod.2015.05.002

Briggs, N., Perry, M. J., Cetinić, I., Lee, C., D'Asaro, E., Gray, A. M., & Rehm, E. (2011). High-resolution observations of aggregate flux during a sub-polar North Atlantic spring bloom. *Deep Sea Research I: Oceanographic Research Papers*, *58*(10), 1031–1039. https://doi.org/10.1016/j.dsr.2011.07.007

Buckingham, C. E., Naveira Garabato, A. C., Thompson, A. F., Brannigan, L., Lazar, A., Marshall, D. P., et al. (2016). Seasonality of submesoscale flows in the ocean surface boundary layer. *Geophysical Research Letters*, *43*(5), 2118–2126. https://doi.org/10.1002/2016GL068009

Callies, J., Ferrari, R., Klymak, J. M., & Gula, J. (2015). Seasonality in submesoscale turbulence. *Nature Communications*, *6*, 6862. https://doi.org/10.1038/ncomms7862

Chelton, D. B., Schlax, M. G., & Samelson, R. M. (2011). Global observations of nonlinear mesoscale eddies. *Progress in Oceanography*, *91*(2), 167–216. https://doi.org/10.1016/j.pocean.2011.01.002

Cram, J. A., Weber, T., Leung, S. W., McDonnell, A. M. P., Liang, J.-H., & Deutsch, C. (2018). The role of particle size, ballast, temperature, and oxygen in the sinking flux to the deep sea. *Global Biogeochemical Cycles*, *32*(5), 858–876. https://doi.org/10.1029/2017GB005710

Dale, T., Rey, F., & Heimdal, B. R. (1999). Seasonal development of phytoplankton at a high latitude oceanic site. *Sarsia*, *84*(5–6), 419–435. https://doi.org/10.1080/00364827.1999.10807347

D'Asaro, E., Lee, C., Rainville, L., Harcourt, R., & Thomas, L. (2011). Enhanced turbulence and energy dissipation at ocean fronts. *Science*, *332*(6027), 318–322. https://doi.org/10.1126/science.1201515

Dever, M. (2020a). *Size-differentiated export flux in different dynamical regimes in the ocean: The data*. Mendeley Data, V1. https://doi.org/10.17632/tr9y4s2534.1

Dever, M. (2020b). *Size differentiated export GBC analysis: Release 1*. https://doi.org/10.5281/zenodo.3908126

DeVries, T., Liang, J.-H., & Deutsch, C. (2014). A mechanistic particle flux model applied to the oceanic phosphorus cycle. *Biogeosciences*, *11*(19), 5381–5398. https://doi.org/10.5194/bg-11-5381-2014

Döös, K., Kjellsson, J., & Jönsson, B. (2013). TRACMASS – A Lagrangian trajectory model. In T. Soomere & E. Quak (Eds.), *Preventive methods for coastal protection* (pp. 225–249). New York, NY: Springer International Publishing. https://doi.org/10.1007/978-3-319-00440-2_7

Ducklow, H. W., Steinberg, D. K., & Buesseler, K. O. (2001). Upper ocean carbon export and the biological pump. *Oceanography*, *14*. https://doi.org/10.5670/oceanog.2001.06

Erickson, Z. K., & Thompson, A. F. (2018). The seasonality of physically driven export at submesoscales in the Northeast Atlantic Ocean. *Global Biogeochemical Cycles*, *32*(8), 1144–1162. https://doi.org/10.1029/2018GB005927

Estapa, M. L., Siegel, D. A., Buesseler, K. O., Stanley, R. H. R., Lomas, M. W., & Nelson, N. B. (2015). Decoupling of net community and export production on submesoscales in the Sargasso Sea. *Global Biogeochemical Cycles*, *29*(8), 1266–1282. https://doi.org/10.1002/2014GB004913

Falkowski, P. G., Barber, R. T., & Smetacek, V. (1998). Biogeochemical controls and feedbacks on ocean primary production. *Science*, *281*(5374), 200–206. https://doi.org/10.1126/science.281.5374.200

Fox-Kemper, B., Ferrari, R., & Hallberg, R. (2008). Parameterization of mixed layer eddies. Part I: Theory and diagnosis. *Journal of Physical Oceanography*, *38*(6), 1145–1165. https://doi.org/10.1175/2007JPO3792.1

Gaillard, F. (2015). *ISAS-13 temperature and salinity gridded fields*. SEANOE. https://doi.org/10.17882/45945

Gaillard, F., Reynaud, T., Thierry, V., Kolodziejczyk, N., & von Schuckmann, K. (2016). In situ-based reanalysis of the global ocean temperature and salinity with ISAS: Variability of the heat content and steric height. *Journal of Climate*, *29*(4), 1305–1323. https://doi.org/10.1175/JCLI-D-15-0028.1

Gruber, N., Lachkar, Z., Frenzel, H., Marchesiello, P., Münnich, M., McWilliams, J. C., et al. (2011). Eddy-induced reduction of biological production in eastern boundary upwelling systems. *Nature Geoscience*, *4*(11), 787. https://doi.org/10.1038/NGEO1273

Harrison, P. J., Whitney, F. A., Tsuda, A., Saito, H., & Tadokoro, K. (2004). Nutrient and plankton dynamics in the NE and NW gyres of the subarctic Pacific Ocean. *Journal of Oceanography*, *60*(1), 93–117. https://doi.org/10.1023/B:JOCE.0000038321.57391.2a

Hoskins, B. J., & Bretherton, F. P. (1972). Atmospheric frontogenesis models: Mathematical formulation and solution. *Journal of the Atmospheric Sciences*, *29*(1), 11–37. https://doi.org/10.1175/1520-0469(1972)029⟨0011:AFMMFA⟩2.0.CO;2

Iversen, M. H., & Ploug, H. (2010). Ballast minerals and the sinking carbon flux in the ocean: Carbon-specific respiration rates and sinking velocity of marine snow aggregates. *Biogeosciences*, *7*(9), 2613–2624. https://doi.org/10.5194/bg-7-2613-2010

Iversen, M. H., & Ploug, H. (2013). Temperature effects on carbon-specific respiration rate and sinking velocity of diatom aggregates - potential implications for deep ocean export processes. *Biogeosciences*, *10*(6), 4073–4085. https://doi.org/10.5194/bg-10-4073-2013

Jackson, G. A., Maffione, R., Costello, D. K., Alldredge, A. L., Logan, B. E., & Dam, H. G. (1997). Particle size spectra between 1 μm and 1 cm at Monterey Bay determined using multiple instruments. *Deep Sea Research I*, *44*(11), 1739–1767. https://doi.org/10.1016/S0967-0637(97)00029-0

Klein, P., & Lapeyre, G. (2009). The oceanic vertical pump induced by mesoscale and submesoscale turbulence. *Annual Review of Marine Science*, *1*(1), 351–375. https://doi.org/10.1146/annurev.marine.010908.163704

Kostadinov, T. S., Siegel, D. A., & Maritorena, S. (2009). Retrieval of the particle size distribution from satellite ocean color observations. *Journal of Geophysical Research*, *114*(C9), C09015. https://doi.org/10.1029/2009JC005303

Levy, M., Bopp, L., Karleskind, P., Resplandy, L., Ethe, C., & Pinsard, F. (2013). Physical pathways for carbon transfers between the surface mixed layer and the ocean interior. *Global Biogeochemical Cycles*, *27*(4), 1001–1012. https://doi.org/10.1002/gbc.20092

Lévy, M., Ferrari, R., Franks, P. J. S., Martin, A. P., & Rivière, P. (2012). Bringing physics to life at the submesoscale. *Geophysical Research Letters*, *39*(14). https://doi.org/10.1029/2012GL052756
Lévy, M., Klein, P., & Treguier, A.-M. (2001). Impact of sub-mesoscale physics on production and subduction of phytoplankton in an oligotrophic regime. *Journal of Marine Research*, *59*(4), 535–565. https://doi.org/10.1357/002224001762842181
Llort, J., Langlais, C., Matear, R., Moreau, S., Lenton, A., & Strutton, P. G. (2018). Evaluating Southern Ocean carbon eddy-pump from biogeochemical-argo floats. *Journal of Geophysical Research: Oceans*, *123*(2), 971–984. https://doi.org/10.1002/2017JC012861
Mahadevan, A. (2016). The impact of submesoscale physics on primary productivity of plankton. *Annual Review of Marine Science*, *8*(1), 161–184. https://doi.org/10.1146/annurev-marine-010814-015912
Mahadevan, A., & Archer, D. (2000). Modeling the impact of fronts and mesoscale circulation on the nutrient supply and biogeochemistry of the upper ocean. *Journal of Geophysical Research*, *105*(C1), 1209–1225. https://doi.org/10.1029/1999JC900216
Mahadevan, A., D'Asaro, E., Lee, C., & Perry, M. J. (2012). Eddy-driven stratification initiates North Atlantic spring phytoplankton blooms. *Science*, *337*(6090), 54–58. https://doi.org/10.1126/science.1218740
Mahadevan, A., Oliger, J., & Street, R. (1996a). A nonhydrostatic mesoscale ocean model. Part II: Numerical implementation. *Journal of Physical Oceanography*, *26*(9), 1881–1900. https://doi.org/10.1175/1520-0485(1996)026⟨1881:ANMOMP⟩2.0.CO;2
Mahadevan, A., Oliger, J., & Street, R. (1996b). A nonhydrostatic mesoscale ocean model. Part I: Well-posedness and scaling. *Journal of Physical Oceanography*, *26*(9), 1868–1880. https://doi.org/10.1175/1520-0485(1996)026⟨1868:ANMOMP⟩2.0.CO;2
Mahadevan, A., & Tandon, A. (2006). An analysis of mechanisms for submesoscale vertical motion at ocean fronts. *Ocean Modelling*, *14*(3–4), 241–256. https://doi.org/10.1016/J.OCEMOD.2006.05.006
McCave, I. (1984). Size spectra and aggregation of suspended particles in the deep ocean. *Deep Sea Research Part I*, *31*(4), 329–352. https://doi.org/10.1016/0198-0149(84)90088-8
McDonnell, A., & Buesseler, K. (2012). A new method for the estimation of sinking particle fluxes from measurements of the particle size distribution, average sinking velocity, and carbon content. *Limnology and Oceanography: Methods*, *10*, 329–346. https://doi.org/10.4319/lom.2012.10.329
McDonnell, A. M. P., & Buesseler, K. O. (2010). Variability in the average sinking velocity of marine particles. *Limnology & Oceanography*, *55*(5), 2085–2096. https://doi.org/10.4319/lo.2010.55.5.2085
McWilliams, J. C. (2016). Submesoscale currents in the ocean. *Proceedings of the Royal Society A: Mathematical, Physical and Engineering Science*, *472*(2189). https://doi.org/10.1098/rspa.2016.0117
Mensa, J. A., Garraffo, Z., Griffa, A., Özgökmen, T. M., Haza, A., & Veneziani, M. (2013). Seasonality of the submesoscale dynamics in the Gulf Stream region. *Ocean Dynamics*, *63*(8), 923–941. https://doi.org/10.1007/s10236-013-0633-1
Mesinger, F., DiMego, G., Kalnay, E., Mitchell, K., Shafran, P. C., Ebisuzaki, W., et al. (2006). North American regional reanalysis. *Bulletin of the American Meteorological Society*, *87*(3), 343–360. https://doi.org/10.1175/BAMS-87-3-343
Omand, M. M., D'Asaro, E. A., Lee, C. M., Perry, M. J., Briggs, N., Cetini, I., & Mahadevan, A. (2015). Eddy-driven subduction exports particulate organic carbon from the spring bloom. *Science*, *348*(6231), 222–225. https://doi.org/10.1126/science.1260062
Omand, M. M., Govindarajan, R., He, J., & Mahadevan, A. (2020). Sinking flux of particulate organic matter in the oceans: Sensitivity to particle characteristics. *Scientific Reports*, *10*(1), 1–16. https://doi.org/10.1038/s41598-020-60424-5
Parsons, T. R., & Lalli, C. M. (1988). Comparative oceanic ecology of the plankton communities of the subarctic Atlantic and Pacific oceans. *Oceanography and Marine Biology an Annual Review*, *26*, 317–359.
Pelland, N. (2018). *Seaglider Surveys at ocean station Papa: Bin-averaged profiles, currents, and independent oxygen data*. Retrieved From http://hdl.handle.net/1773/41656
Pelland, N., Eriksen, C., & Cronin, M. (2016). Seaglider surveys at Ocean Station Papa: Circulation and watermass properties in a meander of the North Pacific current. *Journal of Geophysical Research: Oceans*, *121*, 6816–6846. https://doi.org/10.1002/2016JC011920
Petrik, C., Jackson, G., & Checkley, D. (2013). Aggregates and their distributions determined from LOPC observations made using an autonomous profiling float. *Deep Sea Research Part I*, *74*, 64–81. https://doi.org/10.1016/j.dsr.2012.12.009
Plant, J. N., Johnson, K. S., Sakamoto, C. M., Jannasch, H. W., Coletti, L. J., Riser, S. C., & Swift, D. D. (2016). Net community production at Ocean Station Papa observed with nitrate and oxygen sensors on profiling floats. *Global Biogeochemical Cycles*, *30*(6), 859–879. https://doi.org/10.1002/2015GB005349
Ploug, H., Iversen, M. H., Koski, M., & Buitenhuis, E. T. (2008). Production, oxygen respiration rates, and sinking velocity of copepod fecal pellets: Direct measurements of ballasting by opal and calcite. *Limnology & Oceanography*, *53*(2), 469–476. https://doi.org/10.4319/lo.2008.53.2.0469
PMEL. (2018). *Pacific Marine Environment Laboratory Ocean Climate Stations Mooring data*. Retrieved From https://www.pmel.noaa.gov/ocs/data-overview
Resplandy, L., Lévy, M., & McGillicuddy, D. J. (2019). Effects of eddy-driven subduction on ocean biological carbon pump. *Global Biogeochemical Cycles*, *33*(8), 1071–1084. https://doi.org/10.1029/2018GB006125
Richardson, T., & Jackson, G. (2007). Small phytoplankton and carbon export from the surface ocean. *Science*, *315*, 838–840. https://doi.org/10.1126/science.1133471
Riley, J., Sanders, R., Marsay, C., Le Moigne, F. A., Achterberg, E. P., & Poulton, A. J. (2012). The relative contribution of fast and slow sinking particles to ocean carbon export. *Global Biogeochemical Cycles*, *26*(1). https://doi.org/10.1029/2011GB004085
Rocha, C. B., Gille, S. T., Chereskin, T. K., & Menemenlis, D. (2016). Seasonality of submesoscale dynamics in the Kuroshio extension. *Geophysical Research Letters*, *43*(21), 11304–11311. https://doi.org/10.1002/2016GL071349
Rudnick, D. L. (2001). On the skewness of vorticity in the upper ocean. *Geophysical Research Letters*, *28*(10), 2045–2048. https://doi.org/10.1029/2000GL012265
Sheldon, R., Prakash, A., & Sutcliffe, W. Jr. (1972). The size distribution or particles in the ocean. *Limnology & Oceanography*, *17*(3), 327–340. https://doi.org/10.4319/lo.1972.17.3.0327
Sherry, N. D., Boyd, P. W., Sugimoto, K., & Harrison, P. J. (1999). Seasonal and spatial patterns of heterotrophic bacterial production, respiration, and biomass in the subarctic NE Pacific. *Deep-Sea Research Part II Topical Studies in Oceanography*, *46*(11–12), 2557–2578. https://doi.org/10.1016/S0967-0645(99)00076-4
Siegel, D. A., Buesseler, K. O., Behrenfeld, M. J., Benitez-Nelson, C. R., Boss, E., Brzezinski, M. A., et al. (2016). Prediction of the export and fate of global ocean net primary production: The exports science plan. *Frontiers in Marine Science*, *3*, 22. https://doi.org/10.3389/fmars.2016.00022
Stukel, M. R., Aluwihare, L. I., Barbeau, K. A., Chekalyuk, A. M., Goericke, R., Miller, A. J., et al. (2017). Mesoscale ocean fronts enhance carbon export due to gravitational sinking and subduction. *Proceedings of the National Academy of Sciences*, *114*(6), 1252–1257. https://doi.org/10.1073/pnas.1609435114

Stukel, M. R., & Ducklow, H. W. (2017). Stirring up the biological pump: Vertical mixing and carbon export in the Southern Ocean. *Global Biogeochemical Cycles*, *31*(9), 1420–1434. https://doi.org/10.1002/2017GB005652

Stukel, M. R., Song, H., Goericke, R., & Miller, A. J. (2018). The role of subduction and gravitational sinking in particle export, carbon sequestration, and the remineralization length scale in the California Current Ecosystem. *Limnology & Oceanography*, *63*(1), 363–383. https://doi.org/10.1002/lno.10636

Taylor, J. R., Smith, K. M., & Vreugdenhil, C. A. (2020). The influence of submesoscales and vertical mixing on the export of sinking tracers in large-eddy simulations. *Journal of Physical Oceanography*, *50*(5), 1319–1339. https://doi.org/10.1175/JPO-D-19-0267.1

Thomas, L. N., Tandon, A., & Mahadevan, A. (2013). Submesoscale processes and dynamics. In M. W. Hecht & H. Hasumi (Eds.), *Ocean modeling in an eddying regime* (pp. 17–38). Washington, DC: American Geophysical Union (AGU). https://doi.org/10.1029/177GM04

Thomas, L. N., Taylor, J. R., Ferrari, R., & Joyce, T. M. (2013). Symmetric instability in the Gulf Stream. *Deep Sea Research Part II: Topical Studies in Oceanography*, *91*, 96–110. https://doi.org/10.1016/j.dsr2.2013.02.025

Thompson, A. F., Lazar, A., Buckingham, C., Naveira Garabato, A. C., Damerell, G. M., & Heywood, K. J. (2016). Open-ocean submesoscale motions: A full seasonal cycle of mixed layer instabilities from gliders. *Journal of Physical Oceanography*, *46*(4), 1285–1307. https://doi.org/10.1175/JPO-D-15-0170.1

Turner, J. T. (2015). Zooplankton fecal pellets, marine snow, phytodetritus and the ocean's biological pump. *Progress in Oceanography*, *130*, 205–248.

van Haren, H., Millot, C., & Taupier-Letage, I. (2006). Fast deep sinking in Mediterranean eddies. *Geophysical Research Letters*, *33*(4), L04606. https://doi.org/10.1029/2005GL025367

Waite, A. M., Stemmann, L., Guidi, L., Calil, P. H. R., Hogg, A. M. C., Feng, M., et al. (2016). The wineglass effect shapes particle export to the deep ocean in mesoscale eddies. *Geophysical Research Letters*, *43*(18), 9791–9800. https://doi.org/10.1002/2015GL066463

White, A. E., Letelier, R. M., Whitmire, A. L., Barone, B., Bidigare, R. R., Church, M. J., & Karl, D. M. (2015). Phenology of particle size distributions and primary productivity in the North Pacific subtropical gyre (Station ALOHA). *Journal of Geophysical Research: Oceans*, *120*(11), 7381–7399. https://doi.org/10.1002/2015JC010897